FULL PAPER

Water Splitting

ADVANCED
FUNCTIONAL
MATERIALS

www.afm-journal.de

Bifunctional Heterostructure Assembly of NiFe LDH Nanosheets on NiCoP Nanowires for Highly Efficient and Stable Overall Water Splitting

Haojie Zhang, Xiaopeng Li, Angelika Hähnel, Volker Naumann, Chao Lin, Sara Azimi, Stefan L. Schweizer, A. Wouter Maijenburg,* and Ralf B. Wehrspohn*

3D hierarchical heterostructure NiFe LDH@NiCoP/NF electrodes are prepared successfully on nickel foam with special interface engineering and synergistic effects. This research finds that the as-prepared NiFe LDH@NiCoP/NF electrodes have a more sophisticated inner structure and intensive interface than a simple physical mixture. The NiFe LDH@NiCoP/NF electrodes require an overpotential as low as 120 and 220 mV to deliver 10 mA cm^{-2} for hydrogen evolution reaction (HER) and oxygen evolution reaction (OER) in 1 M KOH, respectively. Tafel and electrochemical impedance spectroscopy further reveal a favorable kinetic during electrolysis. Specifically, the NiFe LDH@NiCoP/NF electrodes are simultaneously used as cathode and anode for overall water splitting, which requires a cell voltage of 1.57 V at 10 mA cm^{-2}. Furthermore, the synergistic effect of the heterostructure improves the structural stability and promotes the generation of active phases during HER and OER, resulting in excellent stability over 100 h of continuous operation. Moreover, the strategy and interface engineering of the introduced heterostructure can also be used to prepare other bifunctional and cost-efficient electrocatalysts for various applications.

1. Introduction

Developing earth-abundant, easily scalable, binder-free, stable and bifunctional electrocatalysts with excellent activity for overall water splitting is a promising strategy for the storage and transport of renewable energy in order to address the increasing energy demands and associated environmental crisis.[1]

Electrochemical water splitting to produce H$_2$ and O$_2$ is one of the most efficient and large-scale energy storage and transport strategies, which transforms electric energy into chemical energy and can be easily integrated with other renewable energies (e.g., solar and wind).[2] However, this process has not been widely used in industrial applications. Water electrolysis consists of two half reactions, namely, the oxygen evolution reaction (OER) and the hydrogen evolution reaction (HER), which normally require two types of catalysts to cover the large overpotential necessary to generate H$_2$ and O$_2$.[3] The state-of-the-art electrocatalysts are currently the noble metal Pt based catalysts for the HER and Ru and Ir based catalysts for the OER.[4] However, their large-scale and widespread applications are seriously limited by the global reserve scarcity and exorbitant price of these noble metals. Driven by these challenges, recently an enormous amount of research efforts has been devoted to develop cost-efficient and easily scalable electrocatalysts for improving the electrolytic efficiency and minimizing the dynamic overpotential.[5] On the other hand, practical utilization of particle catalysts involves the usage of binder additives for firmly attaching particles onto the current collector, resulting in limited activity and stability. Therefore, there are considerable efforts focusing on preparing

H. Zhang, Dr. S. L. Schweizer, Prof. R. B. Wehrspohn
Institute of Physics
Martin Luther University Halle-Wittenberg
Heinrich Damerow Str. 4, 06120 Halle (Salle), Germany
E-mail: ralf.b.wehrspohn@imws.fraunhofer.de
Prof. X. Li, C. Lin
CAS Key Laboratory of Low-Carbon Conversion Science and Engineering
Shanghai Advanced Research Institute
Chinese Academy of Sciences (SARI-CAS)
No. 100 Haike Road, 201210 Shanghai, China
Dr. A. Hähnel, Prof. R. B. Wehrspohn
Fraunhofer Institute for Microstructure of Materials and Systems (IMWS)
Walter-Hülse-Str. 1, 06120 Halle (Salle), Germany

Dr. V. Naumann
Fraunhofer-Center for Silicon Photovoltaics (CSP)
Otto-Eißfeldt-Straße 12, 06120 Halle (Saale), Germany
Dr. S. Azimi
Max Planck Institute of Microstructure Physics
Weinbergweg 2, 06120 Halle (Saale), Germany
Prof. A. W. Maijenburg
ZIK SiLi-nano
Martin Luther University Halle-Wittenberg
Karl-Freiherr-von-Fritsch-Str. 3, 06120 Halle (Salle), Germany
E-mail: wouter.maijenburg@chemie.uni-halle.de

ADVANCED
SCIENCE NEWS
www.advancedsciencenews.com

ADVANCED
FUNCTIONAL
MATERIALS
www.afm-journal.de

binder-free and bifunctional electrodes that are cost efficient and obtain high catalytic activity by reduction of the overpotential for HER and OER.[6] Furthermore, the binder-free and bifunctional electrodes can simplify the design and construction of the electrolysis device.

Previous research has indicated that adequate structure design not only accelerates the performance of electrolysis by improving the charge transfer capability between catalysts and substrate, but also provides the possibility to combine two different kinds of catalysts for the preparation of bifunctional electrocatalysts for overall water splitting.[7] For instance, Yang et al. prepared MoS_2-Ni_2S_2 heteronanorods on nickel foam (NF), which exhibited a cell voltage of 1.50 V at 10 mA cm^{-2} for overall water splitting.[8] Xiao et al. electrodeposited amorphous NiFe nanosheets on $NiCo_2O_4$ nanoflakes as a bifunctional electrocatalyst for HER and OER.[9] Hou et al. prepared ternary hybrid CoSe/NiFe LDH/EG by depositing NiFe LDH (layered double hydroxide) on the in situ grown NiSe nanosheets vertically oriented on exfoliated graphene foil.[10] Wang et al. molecularly coupled NiFe LDH nanosheets on $NiCo_2O_4$ nanowire arrays on an NF substrate, which was used as a bifunctional electrocatalyst for overall water splitting.[11] Zhang et al. studied the interface engineering of the MoS_2/Ni_3S_2 heterostructure as a bifunctional electrocatalyst with accelerated overall water splitting performance.[7] Furthermore, Liu et al. fabricated the heterostructure by combining NiFe LDH nanosheets with in situ grown $NiCo_2S_4$ nanotubes on NF with an enhanced overall water splitting activity.[12] Previous approaches revealed that electrocatalysts with appropriate design of the heterostructure can result in promising bifunctional activity for water splitting. On the other hand, metal phosphides have recently attracted extensive research interest owing to their high activity.[13] However, their relatively poor OER performance, compared to state-of-the-art non-noble metal OER catalysts such as NiFe LDH, limited their application as bifunctional electrocatalysts for water splitting and only a few bifunctional heterostructure metal phosphides have been reported so far.[14] Therefore, it is expected that the formation of a heterostructure by combining metal phosphides with NiFe LDH, which is a promising electrocatalyst for OER, will be a promising strategy for the preparation of active bifunctional electrocatalysts for water splitting.

Herein, we present a 3D hierarchical heterostructure NiFe LDH@NiCoP/NF constructed by coupling ultrathin NiFe LDH with NiCoP nanowires by a simple three-step hydrothermal–phosphorization–hydrothermal process at low temperature. This structure showed a synergistically enhanced performance for HER and OER. For the preparation of these 3D hierarchical NiFe LDH@NiCoP/NF heterostructures, we first hydrothermally grew NiCo hydroxide nanowires on the NF, which had a porous 3D structure beneficial for releasing the formed H_2

and O_2 gas bubbles and which can be used as the current collector. Afterward, these NiCo hydroxide nanowires were phosphatized for the formation of NiCoP nanowires. Finally, NiFe LDH nanosheets were grown on top of these NiCoP nanowires by an additional hydrothermal reaction. The as-synthesized NiFe LDH@NiCoP/NF electrodes with engineered interface exhibited synergistic effects toward electrocatalytic reactions. Therefore, the NiFe LDH@NiCoP/NF required overpotentials as low as 120 and 220 mV to achieve 10 mA cm^{-2} for HER and OER, respectively, and excellent stability for 100 h. The NiFe LDH@NiCoP/NF electrodes also possessed a lower Tafel slope, smaller charge transfer resistance (R_{ct}), and higher electrochemically active surface area (ECSA) as compared to NiFe LDH/NF and NiCoP/NF. Specifically, the NiFe LDH@NiCoP/NF electrodes were used as cathode and anode for overall water splitting resulting in a cell voltage of 1.57 V to achieve 10 mA cm^{-2} with outstanding durability for 100 h, making it become one of the most efficient earth-abundant bifunctional electrocatalysts for overall water splitting. Overall, 3D hierarchical heterostructure electrodes made of earth-abundant metals were prepared successfully for overall water splitting. Additionally, we also provided mechanistic insights into the impact of heterostructure interfaces.

2. Results and Discussion

The NiFe LDH@NiCoP/NF electrodes were prepared by a simple three-step hydrothermal–phosphorization–hydrothermal method according to previous reports.[9,14b] The schematic diagram in **Figure 1** illustrates the processes used for the preparation of the hierarchical heterostructure NiFe LDH@NiCoP supported on NF. NF was used as a 3D porous binder-free substrate that provided sufficient mechanical strength and conductivity. The X-ray diffraction (XRD) spectrum of the as-prepared NiFe LDH@NiCoP/NF is shown in **Figure 2**a, together with bare NF, NiCoP, and NiFe LDH/NF as references, for interpreting the structure information. From the pattern of NiFe LDH@NiCoP/NF, the peaks located a 2θ = 44.5°, 51.9°, and 76.37° can be assigned to the (111), (200), and (220) planes of Ni, respectively (PDF #04-0850), and the peaks at 2θ = 40.9°, 45.6°, and 54.4° well matched with the (111), (210), and (300) planes of NiCoP, respectively (PDF #71-2336), while the peaks at 2θ = 11.7°, 23.2°, 33.2°, 38.7°, and 61.3° coincided very well with the (003), (006, (101), (015), and (113) planes of the NiFe LDH, respectively, as observed by NiFe LDH/NF and NiCoP/NF as well.[11,14b]

From the scanning electron microscopy (SEM) images shown in Figure S1a,b of the Supporting Information, the revealed NF had a 3D open porous structure with enough space for the
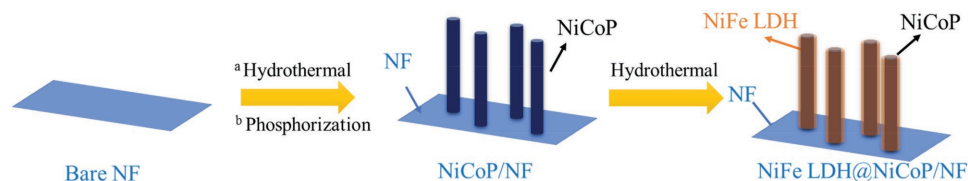

Figure 1. Schematic representation of the synthesis of 3D hierarchical NiFe LDH@NiCoP/NF electrodes.
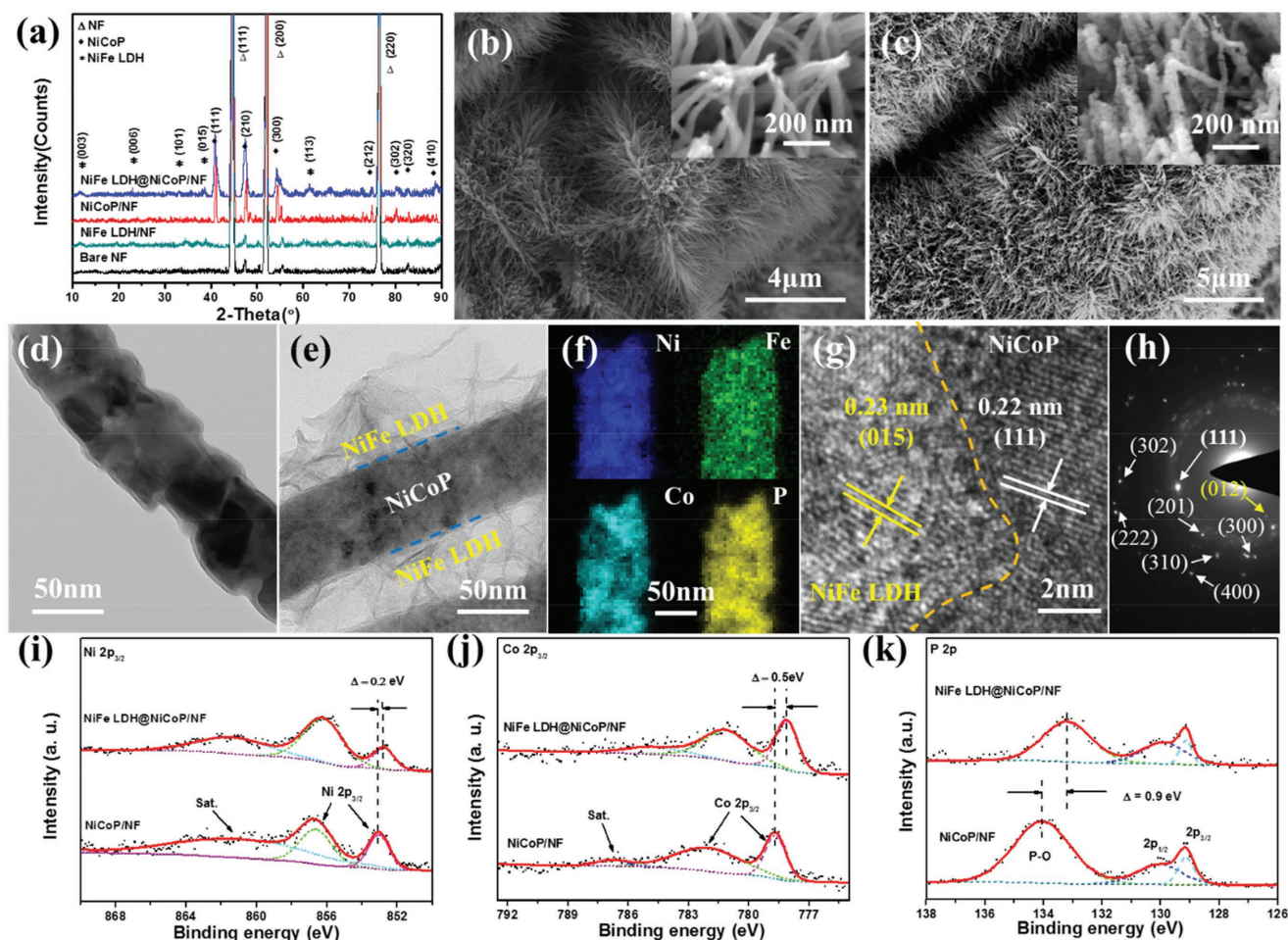
Figure 2. a) XRD spectra of the bare NF, NiCoP/NF, NiFe LDH@NiCoP/NF, and NiFe LDH/NF. b) SEM image of the as-synthesized NiCoP/NF nanowires, where the inset shows a high-resolution image of the NiCoP nanowires. c) SEM image of the as-synthesized NiFe LDH@NiCoP/NF nanowires, where the inset shows a high-resolution image of the NiFe LDH@NiCoP nanowires. d) TEM image of an NiCoP nanowire. e) TEM image of an NiFe LDH@NiCoP nanowire. f) EDX mapping images of the NiFe LDH@NiCoP nanowire. g) HRTEM image of the NiFe LDH@NiCoP nanowire highlighting the interface between nanowire and nanosheets. h) SAD pattern of the interface of the NiFe LDH@NiCoP. i–k) XPS patterns of the Ni $2p_{3/2}$, Co $2p_{3/2}$, and P 2p for NiCoP/NF and NiFe LDH@NiCoP/NF, respectively.

release of the generated O_2 and H_2 gas bubbles. Furthermore, the surface of the NF is smooth and the energy dispersive X-ray spectroscopy (EDX) spectrum (Figure S1c, Supporting Information) indicated that Ni and O were the only elements existing in the NF. After the first hydrothermal reaction, NiCo hydroxide nanowires were uniformly grown on the surface of NF as shown in Figure S1d,e of the Supporting Information, and the EDX pattern shown in Figure S1f of the Supporting Information confirmed the presence of Ni and Co. Figure 2b shows the morphology of the NiCoP nanowires, which was preserved after phosphorization (inset image). The EDX spectrum as shown in Figure S2a and Table S1 of the Supporting Information verified the presence of Ni, Co, and P. As displayed in Figure 2c, the NiFe LDH@NiCoP nanowires exhibited a heterostructure with ultrathin NiFe LDH nanosheets grown around the surface of the NiCoP nanowires supported on the NF substrate. From the EDX pattern of the as-prepared NiFe LDH@NiCoP/NF, the peaks from Co, Ni, Fe, and P were clearly discernible and the ratio of Ni:Co:P:Fe is 33:22:22:1 (as shown in Figure S2b and

Table S1 of the Supporting Information). In order to further understand the processes of the growth of NiFe LDH nanosheets, samples consisting of NiFe LDH on NF (denoted as NiFe LDH/NF) were also prepared by the same procedure. After hydrothermal reaction, NiFe LDH ultrathin nanosheets were grown on the NF as shown in Figure S1g,h of the Supporting Information, for which the XRD pattern matched well with the results reported in the literature.[10,15] EDX results indicated that the ratio of Ni:Fe is ≈4:1 as shown in Figure S1i and Table S1 of the Supporting Information.

Transmission electron microscopy (TEM) was used to further investigate the morphology as well as the interfaces between the NiCoP nanowires and NiFe LDH nanosheets. As shown in Figure 2d, the TEM image of an NiCoP nanowire revealed its polycrystalline nature. Figure 2e shows the morphology of an NiFe LDH@NiCoP nanowire and the EDX mapping images (Figure 2f) evidenced the uniform distribution of the elements Ni, Co, P, and Fe throughout the heterostructure. As shown in the high-resolution TEM image (HRTEM) of the NiFe

**ADVANCED
SCIENCE NEWS**
www.advancedsciencenews.com

**ADVANCED
FUNCTIONAL
MATERIALS**
www.afm-journal.de

LDH@NiCoP nanowire (Figure 2g), the interface of the NiCoP nanowire and the NiFe LDH exhibited lattice spacings of 0.22 and 0.23 nm, respectively, which are consistent with the (111) and (012) planes of NiCoP and NiFe LDH, respectively. Selected area (electro) diffraction (SAD) in Figure 2h further confirmed the heterostructure, in line with the XRD results. These results indicated that the as-prepared NiFe LDH@NiCoP/NF electrode had a sophisticated inner structure and interaction.

X-ray photoelectron spectroscopy (XPS) was carried out to probe the surface composition and the corresponding oxidation states of the elements for investigating the synergistic effect of the heterostructure. The Ni $2p_{3/2}$ peaks of the NiCoP/NF are shown in Figure 2i, three peaks at binding energies of 853.0, 856.6, and 861.5 eV were observed, which can be assigned to Ni-P (Ni^{2+}), Ni-PO$_x$ (Ni^{3+}), and satellite peak, respectively.[14b,16] The Ni-P and Ni-PO$_x$ peaks can also be observed for NiFe LDH@NiCoP/NF, which confirmed that the NiFe LDH nanosheets did not completely block the XPS signal of the NiCoP nanowires in the heterostructure. It is noteworthy that the shoulder peak of Ni $2p_{3/2}$ of NiFe LDH@NiCoP/NF located at 852.8 eV (Figure 2i), which is very close to that of metallic Ni (852.6 eV). This suggested that part of the Ni^{2+} has been further reduced during the growth of NiFe LDH.[14b,16] Similarly, the Co $2p_{3/2}$ spectra (Figure 2j) of the NiCoP/NF and NiFe LDH@NiCoP/NF displayed an extra peak located at 778.8 and 778.3 eV, respectively, which can be assigned to the formation of Co-P.[17] Compared with metallic Co (778.2 eV), this peak shifted to slightly higher binding energy, suggesting the presence of partially charged Co species.[18] Moreover, the peaks located at 781.9 and 781.2 eV for NiCoP/NF and NiFe LDH@NiCoP/NF, respectively, can be related to Co-PO$_x$.[13c] After coupling with the NiFe LDH ultrathin nanosheets, the Ni $2p_{3/2}$

and Co $2p_{3/2}$ peaks shifted ≈0.2 and ≈0.5 eV to lower binding energies, respectively, indicating of the strong electronic interactions at the interface between the NiFe LDH nanosheets and the NiCoP nanowires.[11] Figure 2k shows the P 2p spectra of the as-prepared NiCoP/NF and NiFe LDH@NiCoP/NF. The two peaks located at 129.1 and 130.0 eV can be assigned to P^{3-}, and the predominant peaks at 134.1 eV for NiCoP/NF and at 133.2 eV for NiFe LDH@NiCoP/NF can be attributed to PO_4^{3-}.[19] Interestingly, the P 2p peak of the NiFe LDH@NiCoP/NF also shifted 0.9 eV toward lower binding energy, again verifying the charge transfer between NiFe LDH and NiCoP. The interaction between NiFe LDH and NiCoP will be beneficial for the reaction dynamics of both HER and OER.[13a,b]

The electrocatalytic HER performance of the NiFe LDH@NiCoP/NF heterostructure was examined in 1 M KOH using a typical three-electrode configuration. The NiFe LDH@NiCoP/NF heterostructure with a geometric area of 1×1 cm^2 was directly used as the working electrode, and Ag/AgCl (3 M KCl) and Pt wire were used as reference and counter electrode, respectively. For comparison, bare NF, NiCoP/NF, NiFe LDH/NF, and 20 wt% Pt/C supported on bare NF with the same catalyst loading (denoted as Pt/C/NF) were also tested under the same conditions. As shown in **Figure 3**a, the as-prepared NiFe LDH@NiCoP/NF heterostructure possessed an excellent HER activity. The overpotential required for $j = -10$ mA cm^{-2} (η_{10}) is as low as 120 mV without iR compensation (acquired from the chronopotentiometry measurement), which is superior to that of bare NF ($\eta_{10} = 295$ mV), NiFe LDH/NF ($\eta_{10} = 250$ mV), and NiCoP/NF ($\eta_{10} = 185$ mV). The significant improvement of the HER activity originated from the strong interaction and efficient synergy between the NiCoP nanowires and NiFe LDH ultrathin nanosheets. The Tafel slope of 88.2 mV dec^{-1} obtained
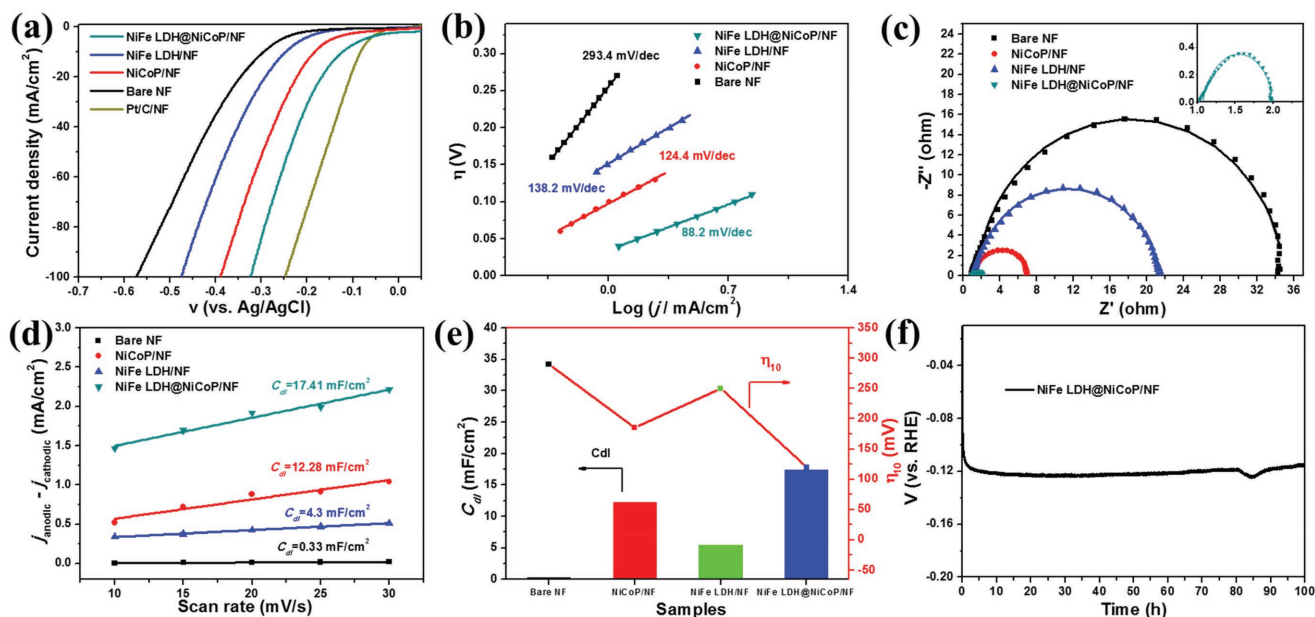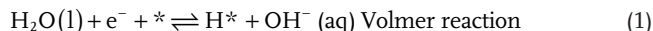

Figure 3. a) Polarization curves of the NiFe LDH@NiCoP/NF, NiCoP/NF, NiFe LDH/NF, Bare NF, and Pt/C/NF for the HER without iR compensation. b) Tafel plots and c) electrochemical impedance spectroscopy for the corresponding electrocatalysts (the magnified impedance pattern for NiFe LDH@NiCoP/NF is shown as inset). d) Plots showing the extraction of the C_{dl} for the estimation of the ECSA. e) The relationship between the C_{dl} and overpotential (η at a current density of -10 mA cm^{-2}). f) Long-time stability test of the NiFe LDH@NiCoP/NF heterostructure for the HER performed at a constant current density of -10 mA cm^{-2}.

**ADVANCED
SCIENCE NEWS**

www.advancedsciencenews.com

**ADVANCED
FUNCTIONAL
MATERIALS**

www.afm-journal.de

for the NiFe LDH@NiCoP/NF heterostructure (Figure 3b) also suggested favorable HER kinetics following the Heyrovsky-step-determined Volmer–Heyrovsky mechanism[20]

$$H_2O(l) + e^- + * \rightleftharpoons H* + OH^- \text{ (aq) Volmer reaction} \quad (1)$$

$$H* + H_2O(l) + e^- \rightleftharpoons H_2(g) + OH^- (aq) + * \text{ Heyrovsky reaction} \quad (2)$$

where * denotes a catalytic site and H* is an adsorbed H-species.

Electrochemical impedance spectroscopy (EIS) measurements were performed to investigate the kinetics of the catalysts at the electrode/electrolyte interface as shown in Figure 3c. All EIS data were fitted with the equivalent circuit as shown in Figure S3 of the Supporting Information, consisting of a resistor (R_1) in series with a parallel combination of a resistor (R_{ct}) and a constant phase element.[21] In this equivalent circuit, R_1 is attributed to the ohmic resistance of the electrolyte, the electrocatalysts, as well as all the contacts, and R_{ct} indicates the charge transfer resistance between the catalysts and the electrolyte. The R_{ct} is related to electrocatalytic kinetics and a lower R_{ct} value corresponds to a faster reaction rate. According to the fitted EIS results (Table S2, Supporting Information), the NiFe LDH@NiCoP/NF heterostructure exhibited the smallest R_{ct} (2.77 Ω), suggesting rapid charge transfer kinetics. This is consistent with the low overpotential and small Tafel slope found for the NiFe LDH@NiCoP/NF. The double layer capacitances (C_{dl}) were measured to estimate the ECSA of all the samples.[14b] As shown in Figure 3d, the C_{dl} of NiFe LDH@NiCoP/NF is ≈32 times higher than that of the bare NF, suggesting that the heterostructure contained many more catalytically active surface sites, which can be attributed to the synthesis of two different types of nanostructures on top of the NF. As seen in Figure 3e, the overpotential decreased along with the increase

of the C_{dl}, which confirmed that the heterostructure offered a higher ECSA for the HER. Stability is another important criterion of electrocatalysts. Figure 3f shows that the NiFe LDH@NiCoP/NF electrode retained its high catalytic activity even after 100 h of continuous operation, which is superior to the activity of most of the recently reported electrocatalysts (usually less than 24 h stability reported). Above results established our NiFe LDH@NiCoP/NF heterostructure as an outstanding HER catalyst with excellent activity as compared to other recently reported earth-abundant HER catalysts in alkaline media (Table S3, Supporting Information).[7,9–12,16,22]

Next to the HER activity, we also investigated the OER activity of the NiFe LDH@NiCoP/NF electrode in 1 M KOH. **Figure 4**a shows the polarization curve of the NiFe LDH@NiCoP/NF without iR compensation (cyan curve). The peaks observed between 1.3 and 1.5 V versus reversible hydrogen electrode (RHE) can probably correspond to the oxidation of M^{2+} to M^{3+} (M = Ni, Co) in the NiFe LDH@NiCoP heterostructure, which was also reported for NiCoP nanowires[23] and NiFe LDH@NiCoS heterostructures.[12] The NiFe LDH@NiCoP/NF electrode exhibited a low overpotential of 220 mV at a current density of 10 mA cm^{-2} (acquired from the chronopotentiometry measurement). In contrast, NiFe LDH/NF, NiCoP/NF, and bare NF required an overpotential of 240, 250, and 330 mV, respectively. Additionally, the NiFe LDH@NiCoP/NF displayed a better OER performance than the state-of-the-art RuO_2 (Figure S4, Supporting Information), owing to its smaller contact resistance and faster charge transfer between the catalyst and the substrate.[24] The excellent OER performance of NiFe LDH@NiCoP/NF is also better than recently reported OER catalysts (Table S4, Supporting Information).[9–12,15b,22,25] Figure 4b shows that the NiFe LDH@NiCoP/NF heterostructure electrode exhibited the smallest Tafel slope of 48.6 mV dec^{-1}, indicating
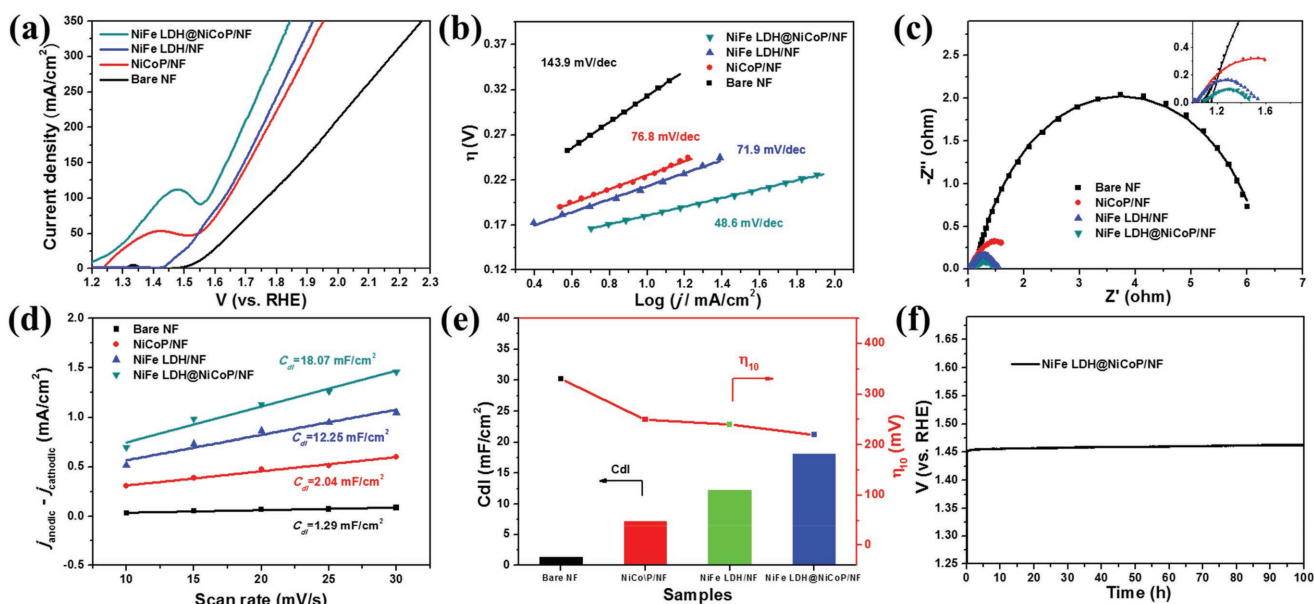

Figure 4. a) Polarization curves of NiFe LDH@NiCoP/NF, NiCoP/NF, NiFe LDH/NF, and bare NF for the OER without iR compensation. b) Tafel plots and c) electrochemical impedance spectroscopy of the corresponding electrocatalysts, the magnified impedance pattern shown as inset. d) Different current density versus scan rate to assess the C_{dl} of the ECSA. e) The relationship between the C_{dl} and overpotential (η at a current density of 10 mA cm^{-2}). f) Long-term stability test of the NiFe LDH@NiCoP/NF for the OER carried out at a constant current density of 10 mA cm^{-2}.

that the NiFe LDH@NiCoP/NF proceeded a faster OER kinetic.[26] The EIS results (Figure 4c and Table S2, Supporting Information) revealed that the NiFe LDH@NiCoP/NF had the smallest R_{ct} (0.41 Ω) among all the samples, indicating a faster charge transfer and favorable reaction kinetics on the heterostructure. The measured C_{dl} of NiFe LDH@NiCoP/NF was much higher than that of NiCoP/NF, NiCo hydroxide/NF, and bare NF (Figure 4d). As shown in Figure 4e, the reduced overpotential for the NiFe LDH@NiCoP/NF heterostructure can be assigned to an increase of the ECSA of the heterostructure as compared to the other samples investigated in this work. To assess the stability of the NiFe LDH@NiCoP/NF electrode

for the OER, a long-time chronopotentiometry measurement was carried out at a current density of 10 mA cm^{-2} for 100 h without observation of degradation (Figure 4f).

In order to further gain insights into the reaction mechanism, the NiFe LDH@NiCoP/NF electrode after HER and OER was characterized by XRD, SEM, TEM, and XPS. For the sample after long-term HER measurement, the crystalline and the morphology remained nearly identical as before, which was evidenced by XRD pattern (Figure S5a, Supporting Information), SEM images (Figure S5b, Supporting Information), and HRTEM images (**Figure 5**a). The dominant O species is metal hydroxide (M-OH) as observed with O 1s
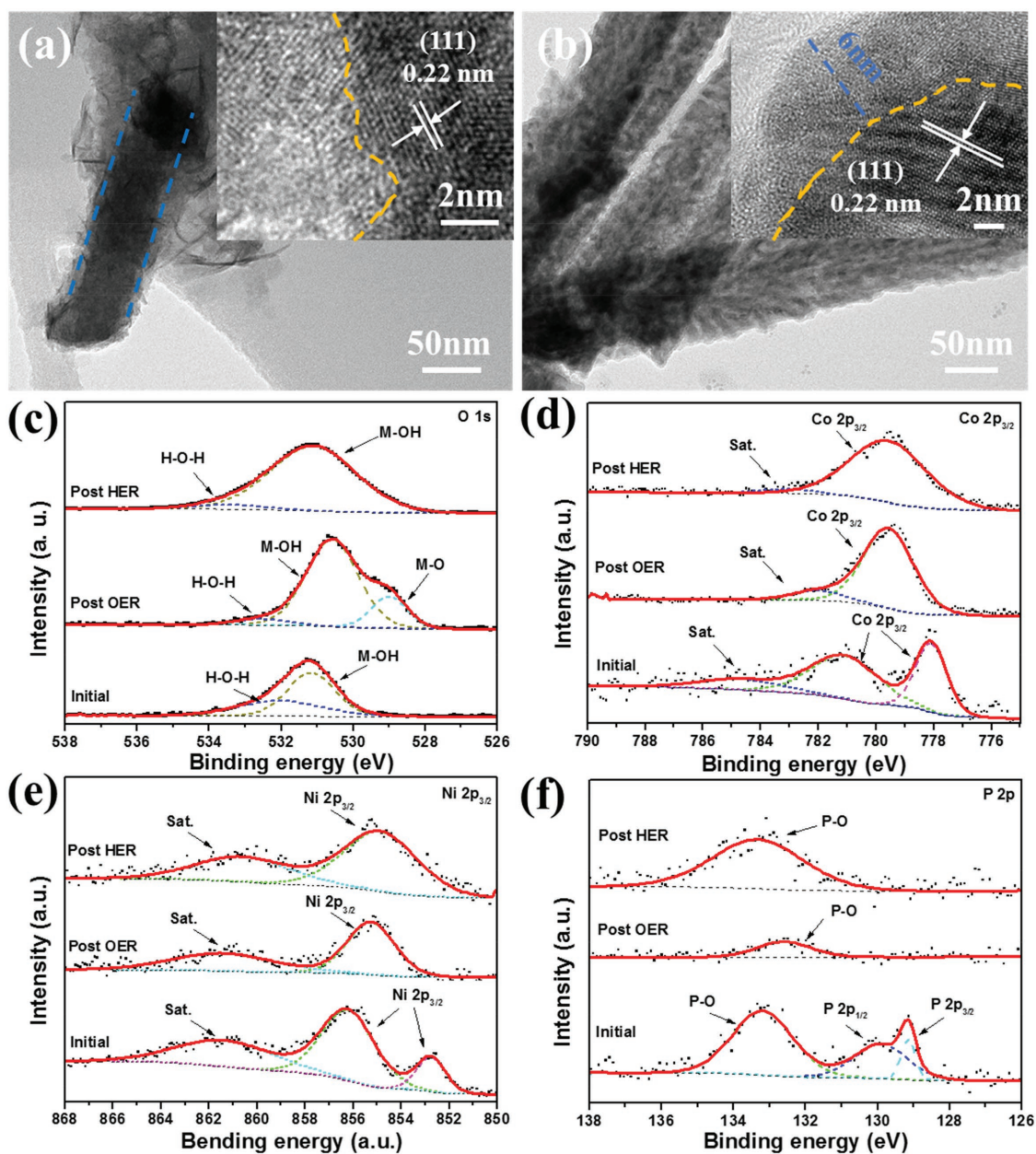

Figure 5. TEM images of the NiFe LDH@NiCoP heterostructure after a) HER and b) OER; the corresponding HRTEM images of the heterostructure are shown in the inset. XPS spectra of the NiFe LDH@NiCoP/NF electrode before reaction, post OER, and post HER. c) O 1s, d) Co 2p$_{3/2}$, e) Ni 2p$_{3/2}$, and f) P 2p, respectively.

**ADVANCED
SCIENCE NEWS**

www.advancedsciencenews.com

**ADVANCED
FUNCTIONAL
MATERIALS**

www.afm-journal.de

spectra (Figure 5c). Meanwhile, the O content (EDX results as shown in Table S1 of the Supporting Information) and the height of the M-OH peak (Figure 5c) increased dramatically, suggesting the formation of a thin metal hydroxide layer on the surface of the heterostructure.[27] It is hard to distinguish this layer from the HRTEM, but it can be validated from the Co $2p_{3/2}$, Ni $2p_{3/2}$, and P 2p spectra of the NiFe LDH@NiCoP/NF after the long-term HER measurement, where the peaks at the low binding energies (Ni ≈852.8 eV, Co ≈ 778.1 eV, and P ≈ 129.2 and 129.9 eV) disappeared as shown in Figure 5d–f.[13a,14b,16] The content of the Fe and P decreased as shown in Table S1 of the Supporting Information, also confirming the formation of the metal hydroxides.

However, the surface morphology of NiFe LDH@NiCoP/NF changed substantially after long-term OER operation. Compared with the HER operating in a reducing potential environment, the strong anodic oxidation in the OER potential range leads to an evident and irreversible phase transformation of metal phosphides to metal oxide/oxyhydroxide. The thickness of the in situ formed oxide/oxyhydroxide layers on the metal phosphides surface was reported in the range of several nanometers.[13b] Here, XRD (Figure S5a, Supporting Information) and SEM (Figure S5c, Supporting Information) characterization suggested that the main crystalline phase and morphology of NiCoP remained after long-term OER measurement. However, The HRTEM images (as shown in Figure 5b) revealed that a new rugged layer with a thickness of ≈6 nm was in situ formed on the surface of the heterostructure. The Fe reduced content change from the EDX (Table S1, Supporting Information) indicated the NiFe LDH was merged together with the newly formed oxide/oxyhydroxide layer. The EDX mapping of the single NiFe LDH@NiCoP (Figure S6, Supporting Information) further confirmed the uniform distribution of the Ni, Co Fe, P, and O on the surface of nanowire. Meanwhile, the O content increased dramatically (as shown in Table S1 of the Supporting Information) and a new peak arose at 529.0 eV in the O 1s spectra (Figure 5c) after long-term OER measurement, further proving the formation of metal oxide/oxyhydroxides.[28] The peaks located at the lower binding energy in the Co $2p_{3/2}$ (Figure 5d) and Ni $2p_{3/2}$ (Figure 5e) spectra disappeared after the OER test, indicating the phase transformation of metal phosphides to metal oxide/oxyhydroxide.[14b] Moreover, this phase transformation can be further confirmed by a dramatic decrease in the P content as shown in Table S1 of the Supporting Information and the lower binding energy peaks disappear in the P 2p spectra as shown in Figure 5f.[14b] These results further confirmed that the surface of NiFe LDH@NiCoP was dominated by the in situ formed metal oxide/oxyhydroxide during OER operation, which has also been regarded as the electrocatalytically active phase.[15b] Overall, owing to the synergistic effect of the strong interface interaction in the heterostructure, the NiFe LDH@NiCoP/NF can maintain the nanowire architecture and crystalline phase of NiCoP. Meanwhile, the surface of the NiFe LDH@NiCoP was enriched with hydroxides (during HER) and oxides/oxyhydroxides (during OER) transformed from NiCoP, which are known as the electrocatalytically active phases.[14d]

According to the results discussed above, the NiFe LDH@NiCoP/NF electrode can serve as an efficient and robust electrocatalyst for HER and OER. Therefore, we also used the NiFe LDH@NiCoP/NF electrodes simultaneously as anode and cathode for overall water splitting as schematically represented in **Figure 6**a. The digital photograph of the electrolytic cell during operation is illustrated in Figure 6b. The video in the Supporting Information recorded at different constant current densities clearly showed the formation of H_2 and O_2 bubbles on the cathode and anode, respectively. The polarization curves (Figure 6c) indicated that the NiFe LDH@NiCoP/NF electrodes exhibited superior overall water splitting activity. Remarkably, a current density of 10 mA cm^{-2} can be achieved with an overpotential as low as 340 mV (calculated from the cell voltage of 1.57 V as acquired during a chronopotentiometry measurement), which is better than or comparable to previously reported electrocatalysts (see Table S5 of the Supporting Information).[6b,9–12,13d,14b,c,22,29] Furthermore, the NiFe LDH@NiCoP/NF showed excellent stability during the long-time overall water splitting measurement with only a slight deactivation during the complete 100 h operation (Figure 6d).

3. Conclusions

In summary, a binder-free bifunctional 3D hierarchical heterostructure electrode consisting of NiFe LDH@NiCoP nanowires on a nickel foam has been successfully prepared through a simple three-step hydrothermal–phosphorization–hydrothermal method for efficient overall water splitting. Our results showed that the NiFe LDH and NiCoP were effectively coupled with strong electronic interaction, leading to facilitated charge transfer and enhanced reaction kinetics. Therefore, this heterostructure can fully utilize the advantage of both components and therefore generate a bifunctional and outstanding electrocatalyst for overall water splitting. The as-prepared NiFe LDH@NiCoP/NF electrodes achieved an excellent performance for both the HER and the OER combined with an outstanding stability in alkaline medium as compared to recently reported earth-abundant electrocatalysts. The enhanced performance of the bifunctional heterostructure was determined by a low overpotential of 120 and 220 mV at a current density of 10 mA cm^{-2} without iR compensation for the HER and the OER, respectively. The overall water splitting of the NiFe LDH@NiCoP/NF electrodes exhibited a cell voltage of 1.57 V to achieve a current density of 10 mA cm^{-2} with excellent stability. According to these results, the heterostructure NiFe LDH@NiCoP/NF electrode is a promising candidate for overall water splitting. Moreover, the synthetic strategy and interface engineering of the heterostructure can also be used to prepare other bifunctional electrocatalysts.

4. Experimental Section

Materials and Chemicals: Iron nitrate nonahydrate (Fe(NO$_3$)$_3$·9H$_2$O, ACS Reagent grade) and nickel nitrate hexahydrate (Ni(NO$_3$)$_2$·6H$_2$O, ACS Reagent grade) were purchased from Merck KGaA. Nickel chloride hexahydrate (NiCl$_2$·6H$_2$O, ≥98%), cobalt chloride hexahydrate (CoCl$_2$·6H$_2$O, ≥98%), ammonium fluoride (NH$_4$F, ≥99.9%), urea (CO(NH$_2$)$_2$, ACS Reagent grade), sodium hypophosphite monohydrate (NaH$_2$PO$_2$·H$_2$O, ≥99%), 20 wt% Pt/C, and Ruthenium(IV) oxide (RuO$_2$, 99.9%) were purchased from Sigma-Aldrich. All the chemicals
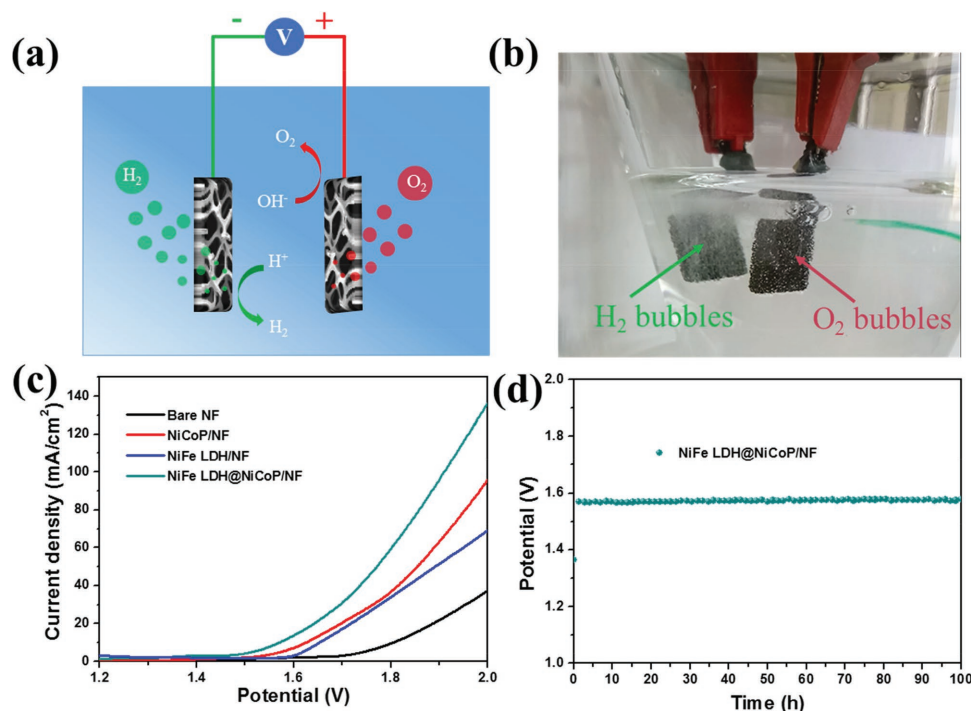
Figure 6. a) Schematic representation of the two-electrode configuration in which an NiFe LDH@NiCoP/NF heterostructure was used as both anode and cathode for overall water splitting. b) Digital photograph of the two-electrode configuration during operation at a constant current density of 100 mA cm^{-2}. c) Polarization curve of as-prepared electrocatalysts. d) Long-term stability test of the NiFe LDH@NiCoP/NF for overall water splitting recorded at a current density of 10 mA cm^{-2} for 100 h.

were used as received without further purification. NF with a thickness of 1.6 mm was purchased from Shanghai Tankii Alloy Material Co., Ltd. and used as the substrate. Ultrapure water with a resistance of 18.2 MΩ, which was purified by a Millipore system (JWT GmbH), was used throughout all experiments.

Synthesis of NiCoP Nanowires on NF (NiCoP/NF): NiCoP nanowires on NF were prepared by a hydrothermal reaction followed by phosphorization. First, 1 mmol CoCl$_2$·6H$_2$O, 0.5 mmol NiCl$_2$·6H$_2$O, 5 mmol urea, and 2.5 mmol NH$_4$F were dissolved in 17.5 mL of water under vigorous stirring for 15 min in order to obtain a clear solution. Second, this solution was transferred to a Teflon-lined stainless steel autoclave and reacted at 120 °C for 6 h with a piece of Ni foam (2.4 cm × 2.4 cm), which was cleaned with acetone, ethanol, a 3 M HCl solution, and pure water under ultrasonication for 15 min each. After reaction, the Teflon-lined stainless steel autoclave was cooled naturally to room temperature and the NF was taken out, washed with water and ethanol, and then dried with an N$_2$ gun. Finally, for phosphorization, 1 g NaH$_2$PO$_2$·H$_2$O was placed at the upstream side of a tube furnace (Carbolite Gero, model E3216) and the NF was placed at the downstream side. Subsequently, the sample was heated to 300 °C in a 500 mL min^{-1} stream of N$_2$ gas for 2 h resulting in NiCoP nanowires on the NF (NiCoP/NF).

Synthesis of NiFe LDH@NiCoP Heterostructure on Ni Foam (NiFe LDH@NiCoP/NF): The NiFe LDH was hierarchically grown on the surface of NiCoP/NF nanowires by employing a second hydrothermal reaction. Typically, the obtained NiCoP/NF was immersed in a 17.5 mL aqueous solution containing 0.25 mmol Fe(NO$_3$)$_2$·6H$_2$O, 0.75 mmol Ni(NO$_3$)$_2$·6H$_2$O, and 1.25 mmol urea in a Teflon-lined stainless steel autoclave, which was hydrothermally treated at 120 °C for 10 h for the growth of the NiFe LDH nanosheets on the surface of the NiCoP nanowires. After the reaction, the autoclave was cooled naturally and the sample was taken out, washed with water and ethanol, and dried with a stream of N$_2$ gas in order to yield the desired heterostructure. The catalyst loadings were determined by weighting the mass of the

NF electrodes before and after catalyst growth. For NiFe LDH@NiCoP/NF in this report, the catalyst loading was ≈2 mg cm^{-2}.

Synthesis of NiFe LDH/NF: For comparison, the NiFe LDH was also directly grown on NF. In a typical procedure, a piece of NF (2.4 cm × 2.4 cm) was cleaned with acetone, ethanol, a 3 M HCl solution and pure water under ultrasonication for 15 min each, and then dried with an N$_2$ gun. Then, it was immersed in a 17.5 mL aqueous solution containing 0.25 mmol Fe(NO$_3$)$_2$·6H$_2$O, 0.75 mmol Ni(NO$_3$)$_2$·6H$_2$O, and 1.25 mmol urea in a Teflon-lined stainless steel autoclave, which was hydrothermally treated at 120 °C for 10 h for the growth of NiFe LDH nanosheets on the surface of the NF (NiFe LDH/NF).

Preparation of 20 wt% Pt/C/NF and RuO$_2$/NF: Samples containing 20 wt% Pt/C and RuO$_2$ were chosen as the benchmark electrocatalyst for the HER and OER for comparison of the H$_2$ and O$_2$ generation activity following the recipe reported previously.[30] Briefly, 5 mg of catalyst was added to a solution containing 750 μL water, 250 μL isopropyl alcohol, and 16 μL 5% Nafion. The obtained suspension was ultrasonicated for 30 min in order to obtain a scattered uniform ink solution. Subsequently, 400 μL of the ink solution was coated on the NF (1 × 1 cm^2) resulting in a catalyst loading of ≈2 mg cm^{-2}. Finally, the samples were dried with hot air.

Characterization: All samples were characterized by XRD using a Bruker D8 diffractometer, with Cu K_α radiation (λ = 1.541874 Å). SEM characterizations were carried out with an FEI Quanta650 FEG scanning electron microscope equipped with an X-ray detector for EDX (Oxford). The morphology of the samples was further characterized by TEM on an FEI Tecnai F20 transmission electron microscopy equipped with an EDX (Oxford). XPS data were obtained by a Kratos Axis Ultra DLD X-ray photoelectron spectrometer equipped with a monochromatic Al K_α X-ray source. All XPS spectra were calibrated by shifting the C 1s peak to 248.8 eV.

Electrochemical Measurements: All electrochemical measurements were conducted using an Autolab PGSTAT302N potentiostat/galvanostat in a typical three-electrode configuration, using a Pt wire and Ag/AgCl reference electrode (3 M KCl) as counter and reference electrode, respectively. The working electrodes were pretreated by 20 cycles of

**ADVANCED
SCIENCE NEWS**

www.advancedsciencenews.com

**ADVANCED
FUNCTIONAL
MATERIALS**

www.afm-journal.de

cyclic voltammetry scans from −1.5 to 1.0 V versus Ag/AgCl (3 M KCl) at 50 mV s^{-1} in 1 M KOH. For the HER and OER performance, the polarization curves were recorded by linear sweep voltammetry at a scan rate of 10 mV s^{-1} in 1 M KOH. For overall water splitting, the prepared electrodes were directly used as cathode and anode in a two-electrode configuration in 1 M KOH at room temperature. For this, the polarization curves were recorded by linear sweep voltammetry from 1.0 to 2.0 V versus the counter electrode at a scan rate of 10 mV s^{-1}. Chronopotentiometry measurements were performed at a constant current density of 10 mA cm^{-2} for 100 h for all relevant reactions: HER, OER, and overall water splitting. The electrochemically active surface areas (ECSA) were estimated by cyclic voltammetry and calibrated according to the method reported by Liang et al.[14b] In short, the double layer capacitance (C_{dl}) was used to indicate the active surface areas for comparison. The currents in a narrow potential window without faradaic processes were measured. Subsequently, the C_{dl} can be estimated by the half slope of the linearly fitted curve of the capacitive current ($\triangle j = j_{anodic} - j_{cathodic}$) plotted against the scan rate. The EIS measurements were recorded at −1.2 V versus Ag/AgCl (3 M KCl) for the HER and 0.55 V versus Ag/AgCl (3 M KCl) for the OER, with a frequency range from 100 kHz to 0.1 Hz and a 10 mV AC dither. All polarization curves were not corrected for iR drop throughout the system. All overpotentials were acquired by chronopotentiometry measurements at a constant current density of 10 mA cm^{-2} for HER, OER, and overall water splitting. All potentials reported in this study for OER and HER were converted to the corresponding potentials versus the RHE using the equation $E_{RHE} = E_{Ag/AgCl} + 0.197 + 0.059 \times$ pH, where E_{RHE} and $E_{Ag/AgCl}$ are the potentials versus RHE and the measured potentials versus Ag/AgCl (3 M KCl) reference electrode, respectively.

Supporting Information

Supporting Information is available from the Wiley Online Library or from the author.

Conflict of Interest

The authors declare no conflict of interest.

[1] H. B. Gray, *Nat. Chem.* **2009**, *1*, 7.
[2] a) M. Caban-Acevedo, M. L. Stone, J. R. Schmidt, J. G. Thomas, Q. Ding, H. C. Chang, M. L. Tsai, J. H. He, S. Jin, *Nat. Mater.* **2015**, *14*, 1245; b) G. Boyle, *Renewable Energy: Power for a Sustainable Future*, Oxford University Press, Oxford **1996**.
[3] C. G. Morales-Guio, L. A. Stern, X. Hu, *Chem. Soc. Rev.* **2014**, *43*, 6555.
[4] X. Li, X. Hao, A. Abudula, G. Guan, *J. Mater. Chem. A* **2016**, *4*, 11973.
[5] a) L. Han, S. Dong, E. Wang, *Adv. Mater.* **2016**, *28*, 9266; b) W. Zhang, W. Lai, R. Cao, *Chem. Rev.* **2017**, *117*, 3717.
[6] a) B. Liu, Y. F. Zhao, H. Q. Peng, Z. Y. Zhang, C. K. Sit, M. F. Yuen, T. R. Zhang, C. S. Lee, W. J. Zhang, *Adv. Mater.* **2017**, *29*, 1606521; b) C. Tang, N. Cheng, Z. Pu, W. Xing, X. Sun, *Angew. Chem., Int. Ed. Engl.* **2015**, *54*, 9351.
[7] J. Zhang, T. Wang, D. Pohl, B. Rellinghaus, R. Dong, S. Liu, X. Zhuang, X. Feng, *Angew. Chem., Int. Ed. Engl.* **2016**, *55*, 6702.
[8] Y. Yang, K. Zhang, H. Lin, X. Li, H. C. Chan, L. Yang, Q. Gao, *ACS Catal.* **2017**, *7*, 2357.
[9] C. Xiao, Y. Li, X. Lu, C. Zhao, *Adv. Funct. Mater.* **2016**, *26*, 3515.
[10] Y. Hou, M. R. Lohe, J. Zhang, S. Liu, X. Zhuang, X. Feng, *Energy Environ. Sci.* **2016**, *9*, 478.
[11] Z. Wang, S. Zeng, W. Liu, X. Wang, Q. Li, Z. Zhao, F. Geng, *ACS Appl. Mater. Interfaces* **2017**, *9*, 1488.
[12] J. Liu, J. Wang, B. Zhang, Y. Ruan, L. Lv, X. Ji, K. Xu, L. Miao, J. Jiang, *ACS Appl. Mater. Interfaces* **2017**, *9*, 15364.
[13] a) X. Wang, R. Tong, Y. Wang, H. Tao, Z. Zhang, H. Wang, *ACS Appl. Mater. Interfaces* **2016**, *8*, 34270; b) L.-A. Stern, L. Feng, F. Song, X. Hu, *Energy Environ. Sci.* **2015**, *8*, 2347; c) H. Huang, C. Yu, J. Yang, C. Zhao, X. Han, Z. Liu, J. Qiu, *ChemElectroChem* **2016**, *3*, 719; d) A. Han, H. Zhang, R. Yuan, H. Ji, P. Du, *ACS Appl. Mater. Interfaces* **2017**, *9*, 2240.
[14] a) N. Jiang, B. You, M. L. Sheng, Y. J. Sun, *Angew. Chem., Int. Ed.* **2015**, *54*, 6251; b) H. Liang, A. N. Gandi, D. H. Anjum, X. Wang, U. Schwingenschlogl, H. N. Alshareef, *Nano Lett.* **2016**, *16*, 7718; c) G.-F. Chen, T. Y. Ma, Z.-Q. Liu, N. Li, Y.-Z. Su, K. Davey, S.-Z. Qiao, *Adv. Funct. Mater.* **2016**, *26*, 3314; d) B. You, N. Jiang, M. Sheng, M. W. Bhushan, Y. Sun, *ACS Catal.* **2016**, *6*, 714.
[15] a) Z. Lu, W. Xu, W. Zhu, Q. Yang, X. Lei, J. Liu, Y. Li, X. Sun, X. Duan, *Chem. Commun.* **2014**, *50*, 6479; b) J. Chi, H. Yu, B. Qin, L. Fu, J. Jia, B. Yi, Z. Shao, *ACS Appl. Mater. Interfaces* **2017**, *9*, 464.
[16] R. Zhang, X. Wang, S. Yu, T. Wen, X. Zhu, F. Yang, X. Sun, X. Wang, W. Hu, *Adv. Mater.* **2017**, *29*, 1605502.
[17] A. W. Burns, K. A. Layman, D. H. Bale, M. E. Bussell, *Appl. Catal., A* **2008**, *343*, 68.
[18] S. Valeri, A. Borghi, G. C. Gazzadi, A. di Bona, *Surf. Sci.* **1999**, *423*, 346.
[19] R. Ye, P. del Angel-Vicente, Y. Liu, M. J. Arellano-Jimenez, Z. Peng, T. Wang, Y. Li, B. I. Yakobson, S. H. Wei, M. J. Yacaman, J. M. Tour, *Adv. Mater.* **2016**, *28*, 1427.
[20] a) B. Losiewicz, *Int. J. Hydrogen Energy* **2004**, *29*, 145; b) A. W. Maijenburg, M. Regis, A. N. Hattori, H. Tanaka, K. S. Choi, J. E. ten Elshof, *ACS Appl. Mater. Interfaces* **2014**, *6*, 2003; c) B. Hinnemann, P. G. Moses, J. Bonde, K. P. Jorgensen, J. H. Nielsen, S. Horch, I. Chorkendorff, J. K. Norskov, *J. Am. Chem. Soc.* **2005**, *127*, 5308.
[21] Y. Wu, G.-D. Li, Y. Liu, L. Yang, X. Lian, T. Asefa, X. Zou, *Adv. Funct. Mater.* **2016**, *26*, 4839.
[22] a) L. L. Feng, G. Yu, Y. Wu, G. D. Li, H. Li, Y. Sun, T. Asefa, W. Chen, X. Zou, *J. Am. Chem. Soc.* **2015**, *137*, 14023; b) M. Ledendecker, S. Krick Calderon, C. Papp, H. P. Steinruck, M. Antonietti, M. Shalom, *Angew. Chem., Int. Ed.* **2015**, *54*, 12361; c) J. Lee, G.-H. Lim, B. Lim, *Chem. Phys. Lett.* **2016**, *644*, 51; d) Q. Liu, S. Gu, C. M. Li, *J. Power Sources* **2015**, *299*, 342; e) J. Luo, J. H. Im, M. T. Mayer, M. Schreier, M. K. Nazeeruddin, N. G. Park,

S. D. Tilley, H. J. Fan, M. Gratzel, *Science* **2014**, *345*, 1593; f) Y. Rao, Y. Wang, H. Ning, P. Li, M. Wu, *ACS Appl. Mater. Interfaces* **2016**, *8*, 33601; g) J. Zhang, T. Wang, D. Pohl, B. Rellinghaus, R. Dong, S. Liu, X. Zhuang, X. Feng, *Angew. Chem.* **2016**, *128*, 6814; h) Z. Y. Zhang, S. S. Liu, F. Xiao, S. Wang, *ACS Sustainable Chem. Eng.* **2017**, *5*, 529.

[23] W. Li, X. Gao, X. Wang, D. Xiong, P.-P. Huang, W.-G. Song, X. Bao, L. Liu, *J. Power Sources* **2016**, *330*, 156.

[24] a) H. Liang, H. N. Alshareef, *Small Methods* **2017**, *1*, 1700111; b) B. Zhang, Y. H. Lui, H. Ni, S. Hu, *Nano Energy* **2017**, *38*, 553.

[25] Q. Xiao, Y. Zhang, X. Guo, L. Jing, Z. Yang, Y. Xue, Y. M. Yan, K. Sun, *Chem. Commun.* **2014**, *50*, 13019.

[26] H. Dau, C. Limberg, T. Reier, M. Risch, S. Roggan, P. Strasser, *ChemCatChem* **2010**, *2*, 724.

[27] X. Wang, W. Li, D. Xiong, D. Y. Petrovykh, L. Liu, *Adv. Funct. Mater.* **2016**, *26*, 4067.

[28] X. Liu, W. Liu, M. Ko, M. Park, M. G. Kim, P. Oh, S. Chae, S. Park, A. Casimir, G. Wu, J. Cho, *Adv. Funct. Mater.* **2015**, *25*, 5799.

[29] a) W. X. Zhu, X. Y. Yue, W. T. Zhang, S. X. Yu, Y. H. Zhang, J. Wang, J. L. Wang, *Chem. Commun.* **2016**, *52*, 1486; b) Y. Yu, P. Li, X. Wang, W. Gao, Z. Shen, Y. Zhu, S. Yang, W. Song, K. Ding, *Nanoscale* **2016**, *8*, 10731; c) R. Xu, R. Wu, Y. Shi, J. Zhang, B. Zhang, *Nano Energy* **2016**, *24*, 103; d) J. Tian, N. Cheng, Q. Liu, X. Sun, Y. He, A. M. Asiri, *J. Mater. Chem. A* **2015**, *3*, 20056; e) T. Liu, Q. Liu, A. M. Asiri, Y. Luo, X. Sun, *Chem. Commun.* **2015**, *51*, 16683; f) D. Liu, Q. Lu, Y. Luo, X. Sun, A. M. Asiri, *Nanoscale* **2015**, *7*, 15122; g) G.-F. Chen, T. Y. Ma, Z.-Q. Liu, N. Li, Y.-Z. Su, K. Davey, S.-Z. Qiao, *Adv. Funct. Mater.* **2016**, *26*, 3314.

[30] H. Zhang, C. Lin, F. Du, Y. Zhao, P. Gao, H. Chen, Z. Jiao, X. Li, T. Zhao, Y. Sun, *ACS Sustainable Chem. Eng.* **2015**, *3*, 2049.

1706847 (10 of 10)